Global tidal impacts of large-scale ice-sheet collapses

Wilmes, Sophie-Berenice; Green, Mattias; Gomez, Matalya; Lau, Harriet; Rippeth, Thomas

Journal of Geophysical Research-Oceans

DOI:
10.1002/2017JC013109

Published: 01/11/2017

Peer reviewed version

Global tidal impacts of large-scale ice-sheet collapses

Sophie-Berenice Wilmes[1,2], J. A. Mattias Green[2], Natalya Gomez[3], Tom P. Rippeth[2], and Harriet Lau[4]

Corresponding author: S.-B. Wilmes, School of Ocean Sciences, Bangor University, Menai Bridge, UK. (s.wilmes@bangor.ac.uk)

[1]College of Earth, Ocean, and Atmospheric Sciences, Oregon State University, Corvallis, USA

[2]School of Ocean Sciences, Bangor University, Menai Bridge, LL59 5AB, UK

[3]Department of Earth and Planetary Sciences, McGill University, 3450 University Street, Montreal, Quebec, Canada

[4]Department of Earth and Planetary Sciences, Harvard University, 20 Oxford Street, Cambridge, USA

Abstract. Recent studies show that the glaciers draining both the West Antarctic and the Greenland ice sheets are experiencing an accelerated ice loss, highlighting the possibility of large-scale ice-sheet retreat and sea-level rise in the coming centuries and millennia. These sea-level changes would vary spatially, and could significantly alter global tides as the latter are highly dependent on bathymetry (or water column thickness under ice shelves) and basin shape. This paper investigates how the principal semi-diurnal (M_2) tidal amplitudes and energy dissipation respond to the non-uniform sea-level changes induced by complete ice-sheet collapses. The sea-level changes are calculated using gravitationally self-consistent sea-level theory, and the tides are simulated using an established tidal model. Results from the simulations show global and spatially heterogeneous changes in tidal amplitudes. In addition, pronounced changes in tidal energy dissipation occur in both the open ocean and in shelf seas, also altering the location of tidal mixing fronts. These changes have the potential to impact ocean mixing, and hence large-scale currents and climate patterns, and the contribution of shelf-sea to the global carbon cycle. The new results highlight the importance of considering changes in the tides in predictions of future climate and reconstructions of past climate phases such as the Last Interglacial.

1. Introduction

Tides play an important role in the global Earth system. They provide energy for abyssal mixing through tidal conversion, which is of importance for the climate-controlling meridional ocean overturning circulation (MOC) [e.g., *Munk and Wunsch*, 1998; *Ledwell et al.*, 2000]. Vertical mixing balances deep water formation and influences the strength of the MOC, thus supporting a key pathway for the redistribution of heat, momentum and freshwater across the globe [e.g., *Wunsch and Ferrari*, 2004; *Green et al.*, 2009]. Tides also sustain the high primary production rates in temperate and polar shelf seas by determining the locations of tidal mixing fronts separating seasonally stratified, nutrient depleted, and fully mixed, nutrient rich waters [*Simpson and Pingree*, 1978]. The location of tidal mixing fronts is controlled by the balance between heating from the sun and mixing by tidal currents and the wind [*Simpson and Hunter*, 1974], meaning that changes in tides can modify the location of the fronts. Tidal conversion is responsible for sustaining a vertical nutrient flux controlling primary production at the shelf break and around seamounts [*Sharples et al.*, 2007], and both tidal mixing fronts and conversion areas are thus valuable fishing grounds as nutrients are resupplied there [e.g., *Sharples et al.*, 2007]. The continental shelf seas also represent a dynamic component of the global carbon budget [*Bauer et al.*, 2013], with the tides playing a key role in mediating seasonally integrated air-sea CO_2 fluxes [*Thomas et al.*, 2004; *Rippeth et al.*, 2008]. In seasonally stratified shelf-sea areas, primary production and respiration are depth-separated by the thermocline. This leads to an increase in remineralized organic carbon and dissolved inorganic carbon from the atmosphere in the subsurface layer. Carbon can subsequently be exported off the

shelf into the deep ocean by horizontal advection or vertical mixing. Seasonally stratified areas therefore act as sinks for CO_2 whereas fully mixed areas are supersaturated with respect to CO_2 and are weak sources of outgassing of CO_2. This process is known as the continental shelf pump [*Tsunogai et al.*, 1999; *Thomas et al.*, 2004; *Rippeth et al.*, 2008].

Because tides propagate as shallow-water waves, they are strongly affected by water-depth (sea-level) changes that can alter the propagation speed of the tidal wave and change the resonant properties of the basin (see e.g. *Green* [2010]). Both sea-level and the areal extent of shelf seas have changed greatly over Earth's history, with associated changes in the tides (see e.g. *Green and Huber* [2013] for the Eocene (∼55 My ago), and *Green et al.* [2017] for tidal changes over the 250 My). However, investigations of the impact of sea-level changes on tides have mostly focused on the Last Glacial Maximum (∼ 25,000 years ago; 'LGM' hereafter) [e.g., *Egbert et al.*, 2004; *Griffiths and Peltier*, 2009; *Green*, 2010; *Wilmes and Green*, 2014] or on regional responses to future sea-level rise [*Ward et al.*, 2012; *Pickering et al.*, 2012; *Pelling and Green*, 2013; *Clara et al.*, 2015; *Carless et al.*, 2016]. *Müller et al.* [2011] attempt to model observed secular changes in the global tides during the late 20th and early 21st century and *Pickering et al.* [2017] simulate tidal responses to sea-level increases expected to occur in the next centuries. Here, we examine the global impacts of sea-level changes induced by large-scale ice-sheet collapses on the tides and associated tidally driven processes.

During the Last Interglacial (∼125 kyr BP; LIG) the West Antarctic Ice Sheet (WAIS) and parts of the Greenland Ice Sheet (GIS) may have collapsed [e.g., *Kopp et al.*, 2009; *Raymo and Mitrovica*, 2012], leading to a sea-level highstand of 6.6–9.4 m relative to present-day levels [*Kopp et al.*, 2009]. Recently, it was highlighted that (partial) ice-sheet

collapses of the WAIS and GIS could occur in the next centuries [e.g., *DeConto and Pollard*, 2016] and are likely in the coming millennia if certain emission thresholds are exceeded [*Clark et al.*, 2016, and references therein]. Glaciers draining the WAIS have shown widespread grounding line retreat [*Rignot et al.*, 2014; *Joughin et al.*, 2014] and increased ice discharge rates [*Mouginot et al.*, 2014] over the last decade. This gives rise to a strongly negative mass balance of the ice sheet [*Velicogna et al.*, 2014]. As the WAIS is a predominately marine-based ice sheet with a reverse bed slope and therefore inherently unstable [*Clark and Lingle*, 1977; *Gomez et al.*, 2010; *Joughin et al.*, 2014], these trends may be linked to the early phases of a marine ice-sheet instability, possibly leading to a collapse of marine sectors of the WAIS in the coming centuries [*Joughin et al.*, 2014; *Mouginot et al.*, 2014]. Together with contributions from the East Antarctic Ice Sheet, this could result in sea-level increase exceeding 10 m by 2300 AD [*DeConto and Pollard*, 2016]. Similarly, the GIS has experienced increased ice mass loss rates over the past decades associated with regionally increased flow speeds [*Velicogna et al.*, 2014]. It has been suggested that if a certain warming threshold is crossed, a full melting of the ice sheet could occur [*Robinson et al.*, 2012; *Clark et al.*, 2016].

A full collapse of an ice sheet would induce globally heterogeneous sea-level changes, due to the loss of the gravitational attraction of the ice sheet, changes in loading of the Earth's surface, and perturbations in the Earth's rotation [*Clark and Lingle*, 1977; *Mitrovica et al.*, 2009; *Gomez et al.*, 2010; *Clark et al.*, 2016, and our Fig. 1–2]. Despite studies showing large, spatially non-unifom sea-level change rates that can have the opposite sign to the global average in some regions [*Clark and Lingle*, 1977; *Mitrovica et al.*, 2009, 2011; *Gomez*

et al., 2010], global responses to large-scale, glacially-mediated sea-level changes in both the future climate and during the LIG have yet to be investigated.

The aims of this study are to demonstrate how collapses of the WAIS or the GIS would impact the tides, and how these impacts could propagate through to key processes and pathways in the global climate system. *Clark et al.* [2016] suggest that, if global greenhouse gas emissions continue at rates similar to present, the Earth will be committed to ice sheet loss from large parts of the WAIS and GIS during the coming millennia and *Kopp et al.* [2009] highlight full or partial ice sheet collapses for the LIG. We deliberately collapse the entire ice sheets to provide the response to the most extreme scenario in order to explore possible tidal changes for the future and for the LIG. All intermediate ice sheet melt cases are likely to evoke tidal changes that lie between the present-day dynamics and these extremes. The sea-level changes are calculated with a gravitationally self-consistent sea-level theory that take into account elastic deformation of the Earth, changes in Earth rotation, and migrating shorelines (see *Gomez et al.* [2010] for details). We first describe the tidal model set-up and forcing data (Section 2). In Section 3 we outline the changes in tidal amplitudes induced by the sea-level changes after a full collapse of the WAIS, the GIS or both. We describe implications for coastal ecosystems and analyze the changes in the dissipation of tidal energy in the oceans and postulate impacts on ocean mixing and shelf sea biogeochemical cycles. The paper concludes with a discussion in Section 4.

2. Simulations and analysis

To demonstrate how collapses of the WAIS or the GIS would impact the tide, and how these impacts could propagate through to key process and pathways in the global climate system, nine numerical tidal model simulations using the forward component of the Oregon

State University Tidal Inversion Software (henceforth OTIS; see [*Egbert et al.*, 2004] for details) were performed. The first was a present day control simulation of the global M_2 tide (see Fig. 3, hereafter 'CTRL'). The second and third simulations implemented a collapsed WAIS (denoted 'No WAIS') and GIS ('No GIS'), respectively, whereas in the fourth simulation both the WAIS and the GIS ('No WAIS & No GIS') were removed. No WAIS, No GIS and No WAIS & No GIS are forced with spatially varying finger-print (FP) sea-level changes. A collapse of the WAIS would lead to a global mean sea-level increase of 5 m [*Mitrovica et al.*, 2011], in the case of the GIS the mean sea-level increase would be 7 m and the collapse of both ice sheets would increase sea-level on average by 12 m. Therefore, additionally, we evaluate the tidal response to a globally uniform sea-level rise. In these simulations sea-level was increased uniformly from the CTRL bathymetry by 5 m, 7 m and 12 m, respectively. These levels correspond to the globally averaged sea-level rise associated with a collapse of the WAIS and/or the GIS. The land-ocean boundaries are held constant with respect to the CTRL for the last three simulations.

2.1. Tidal model

OTIS is widely used for both global and regional modeling of past, present and future ocean tides [e.g., *Egbert et al.*, 2004; *Green*, 2010; *Pelling and Green*, 2013; *Green and Huber*, 2013; *Wilmes and Green*, 2014; *Green et al.*, 2017]. Compared with other unconstrained purely hydrodynamic tidal models, OTIS produces high accuracies both in the open ocean and in coastal regions [*Stammer et al.*, 2014], and is computationally efficient. It solves the shallow-water equations [e.g., *Hendershott*, 1977] neglecting the non-linear advection and diffusion terms without loss of accuracy [*Egbert et al.*, 2004]. The governing

equations are given by

$$\frac{\partial \mathbf{U}}{\partial t} + \mathbf{f} \times \mathbf{U} = -gH\nabla(\zeta - \zeta_{EQ} - \zeta_{SAL}) - \mathbf{F} \tag{1}$$

$$\frac{\partial \zeta}{\partial t} = -\nabla \cdot \mathbf{U} \tag{2}$$

where: $\mathbf{U}$ is the depth integrated volume transport; H is water depth; the tidal current velocity $\mathbf{u}$ is $\mathbf{u} = \mathbf{U}/H$; f is the Coriolis vector; g denotes the gravitational constant; ζ stands for tidal elevation; ζ_{SAL} denotes the tidal elevation due to self-attraction and loading (SAL); and ζ_{EQ} is the equilibrium tidal elevation. $\mathbf{F} = \mathbf{F}_B + \mathbf{F}_w$ represents frictional losses due to quadratic bed friction ($\mathbf{F}_B$) and linear tidal conversion ($\mathbf{F}_w$). The former is represented by the standard quadratic law:

$$\mathbf{F}_B = C_d \mathbf{u}|\mathbf{u}| \tag{3}$$

where $C_d = 0.003$ is a drag coefficient, and $\mathbf{u}$ is the total velocity vector for all the tidal constituents. The conversion, $\mathbf{F}_w = C\mathbf{U}$, includes a conversion coefficient C, which is here defined as [*Zaron and Egbert*, 2006; *Green and Huber*, 2013]

$$C(x, y) = \gamma \frac{(\nabla H)^2 N_b \bar{N}}{8\pi\omega} \tag{4}$$

Here, $\gamma = 50$ is a scaling factor (see *Zaron and Egbert* [2006] for more details), N_b is the buoyancy frequency at the sea-bed (taken from coupled climate model outputs), $\bar{N}$ is the vertical average of the buoyancy frequency, and ω is the frequency of the tidal constituent under evaluation.

Equations (1)–(2) are solved on an Arakawa C-grid, using explicit finite differences time stepping and forcing provided by the astronomic tide generating force (represented by ζ_{EQ} in Eq. (1)). This is followed by harmonic analysis of the steady state solution to obtain tidal elevations and transports. Throughout this study simulations are carried out for M_2

and K_1 only to reduce the computational expense with only very minor losses in accuracy [*Egbert et al.*, 2004].

We used a grid spacing of 1/8°× 1/8° for our OTIS simulations, the same as in *Wilmes and Green* [2014]. This is a compromise between computational efficiency and numerical accuracy; *Egbert et al.* [2004] show that increasing the grid resolution of the model from 1/8° to 1/12° results only in very minor improvements in the model accuracy. The domain used was near global, spanning 86°S–89°N in latitude. This means that the southern open boundary lies over the Antarctic continent, thus eliminating any errors at boundaries. At the northern open boundary elevation boundary conditions are prescribed from the TPXO7.2 database (see *Egbert and Erofeeva* [2002] and `http://volkov.oce.orst.edu/tides/global.html` for more details). The model is run with a time step of 1 s for 13 days of which the last 5 days are used for harmonic analysis with the inbuilt OTIS harmonic analysis software. Four SAL iterations were carried out following the methodology detailed in *Egbert et al.* [2004].

2.2. Bathymetry and sea-level model

Global bathymetric data from *Wilmes and Green* [2014] is used as input to the tidal model for the CTRL scenario. This bathymetry uses ETOPO1 bathymetry [*Amante and Eakins*, 2009] around Antarctica and includes the effects of floating ice shelves around Antarctica on water column thickness by reducing water depth by 0.9×ice thickness from the ETOPO1 database which accounts for the density differences between ice and water. The difference in extent between grounded ice and the total ice extent can be seen in 1. For the No WAIS and No GIS scenarios, the ice in West Antarctica and on Greenland, respectively, is removed and replaced by bedrock data from the ETOPO1 database. Pre-

dicted sea-level changes for collapses of the WAIS or GIS are then added to this initial bathymetry (see e.g. *Bamber and Riva* [2010] for this method) to produce the bathymetry used in the tidal modeling keeping the land-ocean boundaries constant apart from in the ice-sheet collapse locations.

The calculations of sea-level change following the full collapses of the WAIS and GIS (see Fig. 2), with globally averaged equivalent eustatic values (EEVs) of 5 m and 7 m for WAIS and GIS, respectively, were performed using the sea-level theory and algorithm described in detail by *Gomez et al.* [2010]. This theory includes gravitational self-consistency, elastic deformation of the solid Earth, and changes in the rotation of the Earth. It allows for migrating shorelines and the inundation with water of sectors freed of marine-based ice. Calculations are performed up to spherical harmonic degree and order 512, and elastic and density structure of the solid Earth is given by the Preliminary Reference Earth Model [*Dziewonski and Anderson*, 1981]. The prediction for the No WAIS scenario comes directly from *Gomez et al.* [2010], while the prediction for the No GIS scenario was calculated applying the same procedure. The current scenarios represent instantaneous sea-level responses to full ice-sheet collapses. For the simulation with collapses of both WAIS and GIS the sea-level changes from No WAIS and No GIS were added together.

In implementing sea-level changes in tidal models one can either assume that the land-sea configuration remains constant or allow new land to flood; however such a choice may lead to large differences in tidal responses [*Pelling et al.*, 2013]. In light of this concern, we have performed simulations both allowing inundation and fixing the land-sea geometry and find that the global patterns are very similar. We conclude that the grid resolution of our model makes inundation unlikely, and, further, we recognize that areas

experiencing large tidal changes are or will likely be protected by flood defenses (as is the case for the European Shelf; see *Pelling and Green* [2014] for details). We therefore suggest that the differences between 'flooding' and 'no-flooding' are best addressed in high resolution regional studies beyond the scope of this paper, and we do not generate new ocean grid cells in our simulations (i.e., we keep the land-sea geometry fixed throughout our simulations) apart for areas experiencing ice loss.

2.3. Shelf-sea stratification

The Simpson-Hunter Stratification Parameter k was calculated as $k = H/u^3$, where H (m) is water depth and u is tidal current velocity in ms^{-2} [*Simpson and Hunter*, 1974]. A value of $log_{10}(k) = 2.5$ was used to mark the transition between mixed and stratified waters, with $log_{10}(k) > 2.5$ representing stratified waters and $log_{10}(k) < 2.5$ mixed waters [*Simpson and Pingree*, 1978].

2.4. Calculation of dissipation

Dissipation was computed following *Egbert and Ray* [2001]. The tidal dissipation D (in Wm^{-2}) is given by the difference between the work done by the tide producing force W, and the divergence of the tidal energy flux, P:

$$D = W - \nabla \cdot P. \tag{5}$$

The work done by the tide is the sum of two work terms and their corresponding frictional losses expressed as

$$W = g\rho_0 \langle \mathbf{U} \cdot \nabla(\zeta_{EQ} + \zeta_{SAL}) \rangle, \tag{6}$$

where rho_0 is mean ocean density and $\langle$ and $\rangle$ denote the time averages. The energy flux P is given by

$$P = g\rho_0\langle \mathbf{U}\zeta \rangle. \tag{7}$$

3. Results

3.1. Validation

The tidal amplitudes of the CTRL simulation were evaluated against the TPXO8 database [*Egbert and Erofeeva*, 2002, ; http://volkov.oce.orst.edu/tides/tpxo8_atlas.html] using a root-mean square error (RMSE), calculated as the sum of the latitudinally weighted square differences between the CTRL simulation and TPXO8. For M_2 we achieve a global RMSE of 7.7 cm, which in the deep ocean, i.e., here taken to be in water deeper than 500 m, drops to 3.8 cm. The total CTRL dissipation is 2.34 TW, with 0.77 TW being lost in the deep ocean. The values for amplitude and dissipation are consistent with values from TPXO8 (in which total and deep dissipation are 2.39 TW and 0.96 TW, respectively). Consequently, we argue that the model is indeed capturing the tidal dynamics well, and we have confidence in the analysis which follows.

3.2. Amplitudes

Large changes in M_2 amplitudes can be seen in both the No WAIS and No GIS simulations when compared to the CTRL simulation (see Fig. 3). In the No WAIS case, tidal amplitudes of up to 1 m occur in the new West Antarctic ocean basin, together with increases of nearly 0.5 m over the central Ross Sea for both the uniform and FP SLR (fingerprint sea-level rise) simulations (Fig. 4 a) in comparison to the CTRL. Amplitudes also increase throughout the Pacific, particularly in the Panama Basin (by up to 0.2 m),

along the west coast of the US, in the Bering Sea (by up to 1.2 m), along the Asian coast of the Pacific (by up to 0.65 m), and along the north Australian coast. Slight decreases in amplitudes in comparison to the CTRL can be seen west of New Zealand, whereas large increases in amplitudes occur in the Coral Sea. The Atlantic sector sees reductions in tidal amplitudes of up to 1.2 m throughout the North Atlantic, with the exception of Hudson Bay, and larger than present tides in the Southern Atlantic, especially on the Patagonian Shelf. The difference in response between a uniform 5 m SLR and the FP SLR is limited to the Southern Hemisphere. The uniform SLR (Fig. 4b) shows only small responses around Antarctica and reduced amplitude changes on the Patagonian Shelf in comparison to the FP (*cf.* panel a and b in Fig. 4).

For the No GIS simulation much larger differences appear between the FP run and the uniform 7m SLR (Fig. 5; note that the color range in Fig. 5 is scaled, relative to Fig. 4, to the global mean SLR for each case). Slightly larger amplitude increases along the margins of the Pacific can be seen in the FP case due to the larger sea-level (SL) increases that occur in the central Pacific. On the Patagonian Shelf the amplitude increases have a greater magnitude, again due to larger sea-level increases that are greater than the global mean. In the North Atlantic the sea-level change patterns differ strongly between the two cases. The FP case shows greater decreases in the central Atlantic and along the east coast of America. In Hudson Bay the amplitude responses for the FP and the uniform SLR scenario have opposite signs. The large differences between the two scenarios can again be explained with the sea-level forcing: in the FP case the sea-level changes throughout the North Atlantic range from approximately 2 m SLR in the mid-latitudes to sea-level decreases exceeding 10 m along the margins of Greenland.

Overall, the No GIS simulation shows a similar picture to the No WAIS run, although there are regional differences between the two scenarios. The amplitude enhancements throughout the Pacific are larger than in No WAIS due to larger sea-level changes in the No GIS simulation – this is true for both the uniform and FP SLR simulations (*cf.* Fig. 5, a and b). The largest differences between No GIS and No WAIS are found around Antarctica where, in the No GIS case, the amplitude differences are small compared to the control because the local bathymetry remains the same as in the control simulation (see Figs 4 and 5). In the Atlantic, for No GIS, greater amplitude increases occur on the Patagonian Shelf than in No WAIS, but we also see more pronounced decreases throughout the North Atlantic, including Hudson Bay. Furthermore, the response on the European Shelf is much weakened in comparison to No WAIS. Globally, amplitudes increase along 62% and 60% of the coastline for No WAIS and No GIS, respectively, whereas 38% and 40% of the coastline experience decreases. These amplitude changes are therefore likely to alter tidal ranges along most coast lines and hence change flooding potential.

In the combined No WAIS & No GIS simulations the response for a uniform 12 m SLR (Fig. 6, middle panel) is severely reduced compared to the sum of the individual uniform simulations with 5 m and 7 m SLR, respectively (middle panels in Figs. 4 and 5). This is in contrast to the combined FP simulation (Fig. 6, top panel), which experiences a response very similar to the sum of the individual simulations (top panels in Figs. 4 and 5). In the FP case amplitudes are strongly enhanced both in the Pacific open ocean and in most shelf seas adjoining this ocean basin in comparison to the uniform simulation. Especially strong enhancements can be seen in the Coral Sea and the Indonesian Seas, and much greater amplitudes also occur in the Bering Sea.

The reason for the large differences between the fingerprint and the uniform simulation in the No WAIS & No GIS case can be explained with the sea-level forcing. For the combined FP simulation the sea-level changes in the central Pacific Ocean amount to over 16 m (see Fig. 2), making them over one third larger than in the uniform simulation. In addition, the bathymetry change due to the removal of the WAIS leads to a further slight increase in amplitudes along the margins of the Pacific.

Solutions of the Taylor problem for shelf-sea tides [*Rienecker and Teubner*, 1980; *Pelling et al.*, 2013] show that amphidromic points shift towards areas of enhanced dissipation, e.g., due to flooding. A shift of one amphidrome then triggers movement of the adjacent amphidromic points (see Fig. 2 in *Pelling et al.* [2013]). For the No WAIS and the No WAIS & GIS cases the removal of the ice sheet results in an increase in dissipation in the newly formed West Antarctic ocean basin leading to an eastward shift of the southernmost amphidromic point located in the Ross Sea, which subsequently triggers a northwest shift of the neighboring amphidrome (top panels in Fig. 4 and 6). The open ocean amphidromes in the Central and North Pacific shift north- and westward towards areas of enhanced dissipation in the West and North Pacific. For the No GIS scenario, the changes in the Central and North Pacific mirror those in the No WAIS case but differ close to Antarctica as dissipation changes here are much smaller. In the South Atlantic the northwestward migration of the amphidrome between South Africa and central South America results in decreases in amplitudes over the Amazon Shelf. In the North Atlantic which is near-resonant at M_2 frequencies small shifts of the amphidromic points in all scenarios are coincide with considerable amplitude changes. It is likely that the increased dissipation on the Patagonian Shelf seen in both scenarios, and for No WAIS also in

the Weddell Sea sector, reduces dissipation in the North Atlantic and its adjoining shelf seas (see Table 1). This effect can also be seen for the No WAIS & No GIS case where the increases in dissipation on the Patagonian Shelf are especially prominent (174%; see Table 1). The North Atlantic is close to resonance at M_2 frequencies with increasing shelf-sea energy losses damping open ocean dissipation (see e.g. *Egbert et al.* [2004] for an elaboration on the damped harmonic oscillator in relation to Atlantic tides). This is analogous to the tidal changes occurring between the LGM and the Holocene when sea-level rose and shelf seas around the Atlantic progressively flooded reducing open ocean dissipation in the Atlantic [e.g., *Wilmes and Green*, 2014].

These results highlight that tidal amplitude changes at a given location are related to both local and far field sea-level changes, and, in particular for the case of No WAIS, to the inundation of sectors freed of marine-based ice (Fig. 1). In the proximity of the ice sheet the sea-level changes are opposite in sign and an order of magnitude or more greater than the EEV (Fig. 2). For example, in Fig. 2 (top panel), showing sea-level changes induced by a collapse of the WAIS with an EEV of 5 m, sea-level falls in the West Antarctic region by up to 87 m. Note that sea-level changes in the proximity of ice loss are highly dependent on the geometry and amount of ice removed [*Mitrovica et al.*, 2011]. Also, the predictions in Fig. 2 are computed for the scenarios in which the WAIS and GIS fully collapse. This result leads to very different responses of the tides between the No WAIS and the No GIS cases in the polar regions. This aspect is not taken into account when using the traditional uniform sea-level rise scenarios and is especially prominent when comparing the No WAIS & No GIS case with the uniform 12 m SLR run. A comparison of the uniform SLR simulations also indicates a non-linearity in the responses to the sea-

level change. The amplitude changes become proportionally weaker with increases in the sea-level change in the uniform cases whereas this is not the case for the FP simulations. Furthermore, in areas where the predicted sea-level change corresponds to the EEV of the respective ice sheet, the tidal response still differs from the uniform case (compare panels a and b in Figs. 4–6), showing that local (shelf-sea) tidal responses are influenced by far-field dynamics. These results emphasize the importance of using geographically variable sea-level change scenarios, as opposed to the traditional approach of applying globally uniform sea-level increases. They also highlight the importance of using correct boundary conditions which take global changes into account when carrying out high-resolution regional studies.

3.3. Dissipation

Pronounced changes in tidal energy dissipation occur throughout the different ocean basins in response to the changes in tidal processes (see Fig. 7, Fig. 8 and Table 1). In the following, "deep" ("shelf") refers to water depths deeper (shallower) than 500 m. The total (deep) globally-integrated dissipation rate from the M_2 tide increases from 2.28 TW (1.02 TW) in the control simulation to 2.46 TW (1.11 TW) in No WAIS and 2.74 TW (1.25 TW) in No GIS. In No WAIS & No GIS total dissipation increases to 3.00 TW (1.32 TW). The globally-integrated deep dissipation rate increases from 1.02 TW in the control simulation to 1.11 TW in No WAIS, 1.25 TW in No GIS and 1.32 TW in No WAIS & No GIS. For all three FP simulations these changes are mainly due to enhanced dissipation in the Pacific (Fig. 7b and Table 1), especially around the Bering Sea (approximately 55° N). There, shelf dissipation increases by 36% and 63% for No WAIS and No GIS, respectively, and by 203% in No WAIS & No GIS (Table 1). In the China Seas (20° N)

dissipation increases by ∼17% in No WAIS, 34% in No GIS and 25% in No WAIS & No GIS). Enhancements also occur north-east of Australia (15° S). With the exception of the Patagonian Shelf (55° S), where 91% more energy is dissipated in No GIS and 174% in No WAIS & No GIS than in the CTRL simulation, dissipation generally drops throughout the Atlantic in all three simulations (Fig. 7d). This includes decreases on the Amazon Shelf (5° N), in the Bay of Fundy (40° N), and on the European Shelf (50° N; around 40% drops in all three FP cases; see Fig. 7). Interestingly, deep-water dissipation (Fig. 7e) in the Atlantic shows little change for either collapse case, whereas strong increases occur throughout the Pacific (Fig. 7 c). The main locations for enhanced deep-water dissipation are the Coral Sea north-east of Australia (20°S–0°S), the Izu-Bonin-Mariana Arc south of Japan (25°N), and the Aleutian Ridge to the south of the Bering Sea (50° N). In No WAIS, dissipation also increases in the West Antarctic ocean basin. Again, in No GIS, larger changes can be seen than in No WAIS compared to the control, and in No WAIS & No GIS they generally follow the same pattern as the other two FP simulations (except close to the ice sheets) but the magnitude changes are generally greater.

The changes in shelf-sea dissipation are predicted to lead to changes in the extent of seasonal stratification in a number of temperate and polar shelf seas (see Table 2 and Fig. 9). Globally, the spatial extent of permanently mixed waters decreases by around 18–25%, corresponding to an increase in stratified waters for both scenarios, but across the different shelf seas the patterns are highly heterogeneous. For example, in the Bering Sea the extent of mixed waters increases by up to 63% in No WAIS & GIS, whereas for the China Seas, decreases of around 30% occur in all three collapse scenarios. For the

Patagonian Shelf the No WAIS case predicts a decrease in mixed waters whereas strong increases can be seen for No GIS and No WAIS & GIS.

4. Discussion

We have investigated the impact of large-scale ice-sheet collapses on the tides and tidally-driven processes. Our results show prominent global changes in both tidal dynamics and tidally-driven processes in response to the removal of the WAIS and the GIS. These results are applicable for changes that may occur in a warming world, and also for the LIG which is often considered an analogy for our climate system in the next few millennia [e.g., *IPCC*, 2013].

We have compared simulations forced with spatially varying sea-level projections computed with a sea level model that includes gravitational, Earth deformational and Earth rotational effects on sea level and migrating shorelines, to simulations forced with the global average SLR associated with the ice loss event, and found large differences both in amplitudes and dissipation of tides between the two.

Our results highlight that the differences in tides are particularly large in the vicinity of regions of ice loss (i.e. local to Greenland and West Antarctica). In these regions, the draw-down of the sea surface and uplift of the solid Earth in response to ice unloading leads to a sea-level fall that departs significantly from the global average value of SLR associated with the ice loss. Therefore, large differences in the bathymetry between the two scenarios are seen in these areas. Intermediate cases between the present-day case and a full ice-sheet collapse will most likely result in tidal responses somewhere between the CTRL simulation and one of the extreme ice-sheet collapse cases. However, the response of the tides may not scale linearly with respect to the global mean sea-level rise since

firstly, the geometry of the ice loss and the associated geometry of the sea level change will evolve during the ice-sheet collapse, and secondly, the tidal responses are not linear with respect to the sea-level change applied (cf. panel b in Figs. 4–6). Future work will consider these intermediate cases.

Most studies looking at impacts of future sea-level changes on tides, especially those with a regional focus, assume a globally uniform sea-level increase and that open-ocean tides interacting with shelf-sea tidal dynamics show no or little change with respect to the present. Our results and those by previous studies (see e.g. *Arbic et al.* [2009] or *Arbic and Garrett* [2010]), however, indicate that open-ocean tidal changes can impact shelf-sea tides and vice versa. Even if the sea-level forcing on the shelf corresponds to the global mean sea-level increase, shelf-sea tidal changes can still be influenced by far-field tidal changes due to deviations from the global mean sea-level change. Therefore, we suggest that regional studies should apply adequate boundary forcing reflecting potential far-field changes in tidal dynamics.

The largest amplitude changes occur along coastlines and are heterogeneous in nature. In particular, the east and west Pacific margins see large increases in tidal amplitudes whereas the amplitude changes along the Atlantic coastline tend to be smaller or even decrease. These changes in tidal amplitudes are likely to affect coastal morphology and intertidal ecosystems (e.g., salt marshes or mangrove swamps) which at present are among the most diverse ecosystems, and important zones of carbon sequestration [e.g., *Saintilan et al.*, 2013]. The present results also imply considerable changes in past tidal amplitudes which could hamper LIG sea-level reconstructions as sea-level index points often rely on tidal amplitudes not varying in magnitude in the past [e.g., *Scourse*, 2013].

The regional changes in the level of tidal energy dissipation in the shelf seas will profoundly affect local water column structure. Despite a global increase in the geographical extent of seasonal stratification, regional changes are highly heterogeneous. In the Yellow and East China seas and on the Patagonian Shelf (except for No WAIS) the extent of seasonally-stratified water is predicted to increase whereas in the Bering Sea (which is home to a globally-important fishery [*FAO*, 2014]), the areal extent is predicted to shrink. In most shelf seas large shifts in the location of the mixing fronts occur for all scenarios. Our results suggest that the tidally driven changes in shelf-sea oceanography could be large enough to significantly impact ecosystems and the cycling of carbon and nutrients via the shelf sea pump in these systems.

The increased deep-water dissipation rates seen for the central and northern Pacific may affect ocean dynamics, climatic patterns, and as a consequence biogeochemical cycles. The enhancements in the Pacific and the Southern Ocean region could intensify abyssal diapycnal mixing and thus influence the overturning circulation in the Pacific and the Antarctic Circumpolar Current [*Munk and Wunsch*, 1998; *Egbert and Ray*, 2001]. This would affect heat and momentum transfer across the globe, as has been hypothesized to have occurred during the LGM [*Green et al.*, 2009; *Schmittner et al.*, 2015] and Eocene [*Green and Huber*, 2013]. Major changes in dissipation are predicted for the Indonesian Seas which could potentially affect the Indonesian Throughflow current, a major transporter of heat and freshwater to the Indian Ocean [*Sprintall et al.*, 2009], with implications for ENSO and the Indian Ocean dipole, and hence regional climate variability [e.g., *Zhou et al.*, 2015].

We have assumed that global ocean stratification remains unaffected by the addition of melt water from the ice sheets despite the potential of it changing the tidal conversion

rates. A sensitivity simulation (not shown) suggests that changing γ in Eq. (4) only has relatively small effects on the response, and for simplicity we do not change the conversion coefficient between simulations.

Kopp et al. [2009] suggest that global mean sea-level during the LIG (Eemian) was around 8 m higher than at present with both the WAIS and GIS contributing to the sea-level increase. As our simulations suggest that tides and tidal processes are very sensitive to ice sheet losses from both the WAIS and the GIS future work should examine tidal dynamics under realistic LIG ice sheet extent and land-ocean configuration, e.g., taking into account work by *Hay et al.* [2014] who show that the duration over which the ice sheet loss occurs during the LIG affects the sea-level fingerprint of the ice loss.

We conclude that past and future changes in sea level have the potential not only to alter sea-level variability (via the tides) but could also lead to important feedbacks in the climate system which could be superimposed on the variations discussed by *Clark et al.* [2016]. We therefore suggest that parameterizations of tidal effects in climate models need to include and accurately represent the impacts of sea-level changes on the tides. Our results also emphasize the need for high-resolution regional tide studies addressing local impacts of sea-level changes on tides, better descriptions of the mechanisms behind these changes, and their feedbacks with different components of the climate system. Furthermore, such simulations should use global simulations as boundary forcing because the previously used arguments of limited back effects in the deep ocean may not hold.

Acknowledgments. SBW received a PhD studentship from Fujitsu through HPC Wales, who also provided computer facilities and is funded through NSF grant 1559153. JAMG acknowledges funding from the Natural Environmental Research Council through

grants NE/F014821/1 and NE/I030224/1. NG is funded by NSERC, a Tier II Canada Research Chair, McGill University and the Canadian Foundation for Innovation (CFI). HL is supported by Harvard University. Discussions with James Scourse provided valuable feedback for the manuscript. Model output from this study can be obtained at https://zenodo.org/record/834464.

References

Amante, C., and B. W. Eakins (2009), Etopo1 1 arc-minute global relief model: Procedures, data sources and analysis, noaa technical memorandum nesdis ngdc-24, *National Geophysical Data Center, NOAA*, p. 19 pp., doi:10.7289/V5C8276M.

Arbic, B. K., R. H. Karsten and C. Garrett (2009), On tidal resonance in the global ocean and the backeffect of coastal tides upon openocean tides, *Atmosphere – Ocean*, *47*(4), 239–266.

Arbic, B. K. and C. Garrett (2010), A coupled oscillator model of shelf and ocean tides, *Continental Shelf Research*, *30*(6), 564-574.

Bamber, J. and R. Riva (2010), The sea level fingerprint of recent ice mass fluxes, *The Cryosphere*, *4*(4), 621–627.

Bauer, J. E., W. J. Cai, P. A. Raymond, T. S. Bianchi, C. S. Hopkinson, and P. A. Regnier (2013), The changing carbon cycle of the coastal ocean, *Nature*, *504*(7478), 61–70.

Carless, S., J. Green, H. Pelling, and S.-B. Wilmes (2016), Effects of future sea-level rise on tidal processes on the patagonian shelf, *Journal of Marine Systems*, *163*, 113–124, doi:10.1016/j.jmarsys.2016.07.007.

Clara, M. L., C. G. Simionato, E. D'Onofrio, and D. Moreira (2015), Future sea level rise and changes on tides in the Patagonian continental shelf, *Journal of Coastal Research*, *31*, 519–535.

Clark, J. A., and C. S. Lingle (1977), Future sea-level changes due to west antarctic ice sheet fluctuations, *Nature*, *269*(5625), 206–209, doi:10.1038/269206a0.

Clark, P. U., A. S. Dyke, J. D. Shakun, A. E. Carlson, J. Clark, B. Wohlfarth, J. X. Mitrovica, S. W. Hostetler, and A. M. McCabe (2009), The last glacial maximum, *Science*, *325*(5941), 710–714, doi:10.1126/science.1172873.

Clark, P. U., J. D. Shakun, S. A. Marcott, A. C. Mix, M. Eby, S. Kulp, A. Levermann, et al. (2016), Consequences of Twenty-First-Century Policy for Multi-Millennial Climate and Sea-Level Change, *Nature Climate Change*, *6*(4), 360–69, doi:10.1038/nclimate2923.

DeConto, R. M., and D. Pollard (2016), Contribution of Antarctica to past and future sea-level rise, *Nature*, *531*, 591–597.

Dziewonski, A. M., and D. L. Anderson (1981), Preliminary reference earth model, *Physics of the Earth and Planetary Interiors*, *25*(4), 297–356, doi:10.1016/0031-9201(81)90046-7.

Egbert, G. D., and S. Erofeeva (2002), Efficient inverse modeling of barotropic ocean tides, *Journal of Atmospheric and Oceanic Technology*, *19*, 183–204.

Egbert, G. D., and R. D. Ray (2001), Estimates of M_2 tidal energy dissipation from Topex/Poseidon altimeter data, *Journal of Geophysical Research*, *106*, 22,475–22,502.

Egbert, G. D., B. G. Bills, and R. D. Ray (2004), Numerical modeling of the global semidiurnal tide in the present day and in the last glacial maximum, *Journal of Geophysical Research*, *109*, C03,003, doi:10.1029/2003JC001,973.

FAO (2014), The state of world fisheries and aquaculture 2014, *Tech. rep.*, Rome.

Gomez, N., J. X. Mitrovica, M. E. Tamisiea, and P. U. Clark (2010), A new projection of sea level change in response to collapse of marine sectors of the antarctic ice sheet, *Geophysical Journal International*, *180*, 623–634.

Green, J. A. M. (2010), Ocean tides and resonance, *Ocean Dynamics*, *60*, doi: 10.1007/s10236-010-0331-1.

Green, J. A. M., and M. Huber (2013), Tidal dissipation in the early Eocene and implications for ocean mixing, *Geophysical Research Letters*, *40*, doi:10.1002/grl.50,510.

Green, J. A. M., C. L. Green, G. R. Bigg, T. P. Rippeth, J. D. Scourse, and K. Uehara (2009), Tidal mixing and the meridional overturning circulation from the Last Glacial Maximum., *Geophysical Research Letters*, *36*, L15,603, doi:10.1029/2009GL039,309.

Green, J. A. M., M. Huber, D. Waltham, J. Buzan, M. Wells (2017), Explicitly modelled deep-time tidal dissipation and its implication for Lunar history, *Earth and Planetary Science Letters*, *461*, 46–53, doi:org/10.1016/j.epsl.2016.12.038.

Griffiths, S. D., and W. R. Peltier (2009), Modeling of polar ocean tides at the Last Glacial Maximum: amplification, sensitivity, and climatological implications, *Journal of Climate*, *22*, 2905–2924, doi:10.1175/2008JCLI2540.1.

Hay, C., J. X. Mitrovica, N. Gomez, J. R. Creveling, J. Austermann, and R. E. Kopp (2014), The Sea-Level Fingerprints of Ice-Sheet Collapse During Interglacial Periods, *Quaternary Science Reviews*, *87*, 60–69, doi:10.1016/j.quascirev.2013.12.022.

Hendershott, M. C. (1977), Numerical models of ocean tides, in *The Sea vol. 6*, pp. 47–89, Wiley Interscience Publication.

IPCC (2013), *Climate Change 2013: The Physical Science Basis. Contribution of Working Group I to the Fifth Assessment Report of the Intergovernmental Panel on Climate Change*, 1535 pp., Cambridge University Press, Cambridge, United Kingdom and New York, NY, USA, doi:10.1017/CBO9781107415324.

Joughin, I., B. E. Smith, and B. Medley (2014), Marine ice-sheet collapse potentially under way for the Thwaites glacier basin, West Antarctica., *Science*, *344*(6185), 735–738, doi:10.1126/science.1249055.

Kopp, R. E., F. J. Simons, J. X. Mitrovica, A. C. Maloof, and M. Oppenheimer (2009), Probabilistic assessment of sea level during the last interglacial stage, *Nature*, *462*(7275), 863–867.

Ledwell, J., E. Montgomery, K. Polzin, L. S. Laurent, R. Schmitt, and J. Toole (2000), Evidence for enhanced mixing over rough topography in the abyssal ocean., *nature*, *403*, 179–182.

Mitrovica, J. X., N. Gomez, and P. U. Clark (2009), The sea-level fingerprint of West Antarctic collapse, *Science*, *323*(5915), 753, doi:10.1126/science.1166510.

Mitrovica, J. X., N. Gomez, E. Morrow, C. Hay, K. Latychev, and M. E. Tamisiea (2011), On the robustness of predictions of sea level fingerprints, *Geophysical Journal International*, *187*(2), 729–742, doi:10.1111/j.1365-246X.2011.05090.x.

Mouginot, J., E. Rignot, and B. Scheuchl (2014), Sustained increase in ice discharge from the Amundsen Sea embayment, West Antarctica, from 1973 to 2013, *Geophysical Research Letters*, *41*(5), 1576–1584, doi:10.1002/2013GL059069.

Müller, M., B. K. Arbic, and J. X. Mitrovica (2011), Secular trends in ocean tides: Observations and model results, *Journal of Geophysical Research*, *116*(C5), C05013, doi:

549 10.1029/2010JC006387.

550 Munk, W., and C. Wunsch (1998), Abyssal recipes II: Energetics of tidal and wind mixing,
551 *Deep-Sea Research*, *45*, 1977–2010.

552 Pelling, H. E., and J. A. M. Green (2013), Sea-level rise, tidal power, and tides in the Bay
553 of Fundy, *Journal of Geophysical Research*, *118*, 1–11.

554 Pelling, H. E., and J. A. M. Green (2014), The impact of sea level rise and flood defences
555 on tides on the european shelf., *Continental Shelf Research*, *85*, 96–105.

556 Pelling, H. E., J. A. M. Green, and S. L. Ward (2013), Sea level rise on shelf sea tides: to
557 flood or not to flood, *Ocean Dynamics*, *63.*, 21–29.

558 Pickering, M. D., N. S. Wells, K. Horsburgh, and J. A. M. Green (2012), The impact on
559 the European Shelf tides by future sea-level rise, *Continental Shelf Research*, 35, 1–15,
560 doi:10.1016/j.csr.2011.11.011.

561 Pickering, M. D., K. J. Horsburgh, J. R. Blundell, J. J.-M. Hirschi, R. J. Nicholls, M.
562 Verlaan, N. C. Wells (2017), The impact of future sea-level rise on the global tides,
563 *Continental Shelf Research*, *in press*, doi:10.1016/j.csr.2017.02.004.

564 Pingree, R., P. Holligan, and G. Mardell (1978), The effects of vertical stability on phy-
565 toplankton distributions in the summer on the northwest european shelf, *Deep Sea*
566 *Research*, *25*(11), 1011–1028, doi:10.1016/0146-6291(78)90584-2.

567 Raymo, M., and J. Mitrovica (2012), Collapse of polar ice sheets during the stage 11
568 interglacial, *Nature*, *483*, 453–456.

569 Rienecker, M., and M. Teubner (1980), A note on frictional effects in Taylor's problems,
570 *Journal of Marine Research*, *38*, 183–191.

Rignot, E., J. Mouginot, M. Morlighem, H. Seroussi, and B. Scheuchl (2014), Widespread, rapid grounding line retreat of Pine Island, Thwaites, Smith, and Kohler glaciers, West Antarctica, from 1992 to 2011, *Geophysical Research Letters*, *41*(10), 3502–3509, doi: 10.1002/2014GL060140.

Rippeth, T. P., J. D. Scourse, K. Uehara, and S. McKeown (2008), Impact of sea-level rise over the last deglacial transition on the strength of the continental shelf co2 pump, *Geophysical Research Letters*, *35*, L24604, doi:10.1029/2008GL035,880.

Robinson, A., R. Calov, and A. Ganopolski (2012), Multistability and critical thresholds of the greenland ice sheet, *Nature Climate Change*, *2*(6), 429–432, doi: 10.1038/nclimate1449.

Saintilan, N. K. R., D. Mazumder, and C. Woodroffe (2013), Allochthonous and autochthonous contributions to carbon accumulation and carbon store in southeastern australian coastal wetlands, *Estuarine, Coastal and Shelf Science*, *128*, 84–92, doi: 10.1016/j.ecss.2013.05.010.

Schmittner, A., J. A. M. Green, and S.-B. Wilmes (2015), Glacial ocean overturning intensified by tidal mixing in a global circulation model, *Geophysical Research Letters*, *42*, doi:10.1002/2015GL0635,610.

Scourse, J. D. (2013), Quaternary sea level and palaeotidal changes: A review of impacts on, and responses of, the marine biosphere in oceanography and marine biology, *Ocenography and Marine Biology: An Annual Review*, *51*, 1–70.

Sharples, J., J. F. Tweddle, J. A. M. Green, M. R. Palmer, Y. N. Kim, A. E. Hickman, P. M. Holligan, C. M. Moore, T. P. Rippeth, J. H. Simpson, and V. Krivtsov (2007), Spring-neap modulation of internal tide mixing and vertical nutrient fluxes at a shelf

edge in summer, *Limnology and Oceanography*, *52*, 1735–1757.

Simpson, J. H., and J. Hunter (1974), Fronts in the irish sea, *Nature*, *250*, 404–406, doi:10.1038/250,404a0.

Simpson, J. H., and R. D. Pingree (1978), Shallow sea fronts produced by tidal stirring, in *Oceanic fronts in coastal processes*, edited by M. J. Bowman and W. E. Esaias, pp. 29–42, Springer, Berlin Heidelberg.

Sprintall, J., S. E. Wijffels, R. Molcard, and I. Jaya (2009), Direct estimates of the indonesian throughflow entering the indian ocean: 2004-2006, *Journal of Geophysical Research*, *114*, C07,001, doi:10.1029/2008JC005257.

Stammer, D., R. D. Ray, O. B. Andersen, B. K. Arbic, W. Bosch, L. Carrre, Y. Cheng, D. S. Chinn, B. D. Dushaw, G. D. Egbert, S. Y. Erofeeva, H. S. Fok, J. A. M. Green, S. Griffiths, M. A. King, V. Lapin, F. G. Lemoine, S. B. Luthcke, F. Lyard, J. Morison, M. Mller, L. Padman1, J. G. Richman, J. F. Shriver, C. K. Shum, E. Taguchi, and Y. Yi (2014), Accuracy assessment of global ocean tide models, *Reviews of Geophysics*, *52*, doi:10.1002/2014RG000,450.

Thomas, H., E. Elkalay, and H. J. W. de Baar (2004), Enhanced open ocean storage of CO_2 from shelf sea pumping, *Science*, *304*, 1005–1008.

Tsunogai, S., S. Watanabe, and T. Suto (1999), Is there a 'continental shelf pump' for the absorption of atmospheric CO_2?, *Tellus*, *51B*, 701–712, doi:10.1034/j.1600-0889.1999.t01-2-00,010.

Velicogna, I., T. C. Sutterley, and M. R. van den Broeke (2014), Regional acceleration in ice mass loss from greenland and antarctica using grace time-variable gravity data, *Geophysical Research Letters*, *41*(22), 8130–8137, doi:10.1002/2014GL061052.

Ward, S. L., J. A. M. Green, and H. E. Pelling (2012), Tidal dynamics and sediment transport on the European Shelf with future climate change, *Ocean Dynamics*, *62*, 1153–1167.

Wilmes, S.-B., and J. A. M. Green (2014), The evolution of tides and tidally driven mixing over 21,000 years, *Journal of Geophysical Research*, *119*, doi:10.1002/2013JC009,605.

Wunsch, C., and R. Ferrari (2004), Vertical mixing, energy, and the general circulation of the oceans, *Annual Review of Fluid Mechanics*, *36*, 281–314, doi: 10.1146/annurev.fluid.36.050,802.122,121.

Zaron, E. D., and G. D. Egbert (2006), Estimating open-ocean barotropic tidal dissipation: The Hawaiian Ridge, *Journal of Physical Oceanography*, *36*, 1019–1035.

Zhou, Q., W. Duan, M. Mu, and R. Feng (2015), Influence of positive and negative indian ocean dipoles on enso via the indonesian throughflow: Results from sensitivity experiments, *Advances in Atmospheric Sciences*, *32*(6), 783–793.

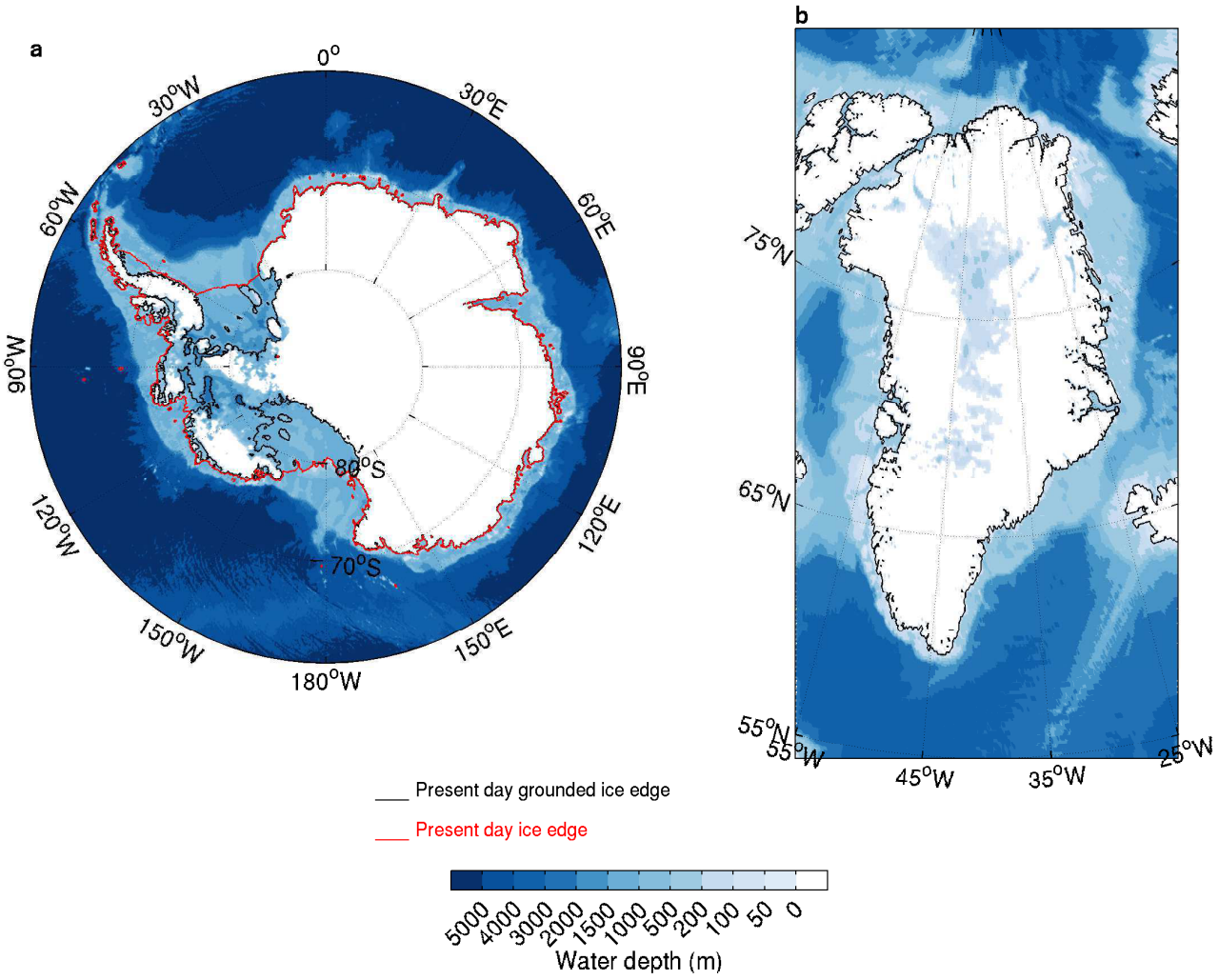

Figure 1. Ocean bathymetry, in meters, with (a) the WAIS and (b) the GIS removed. The white shading indicates land areas or areas of ice higher than the sea surface height, whereas the black line shows the present day ice-sheet grounding line. For the No WAIS case the present-day ice sheet extent is additionally shown as floating ice shelves are present.

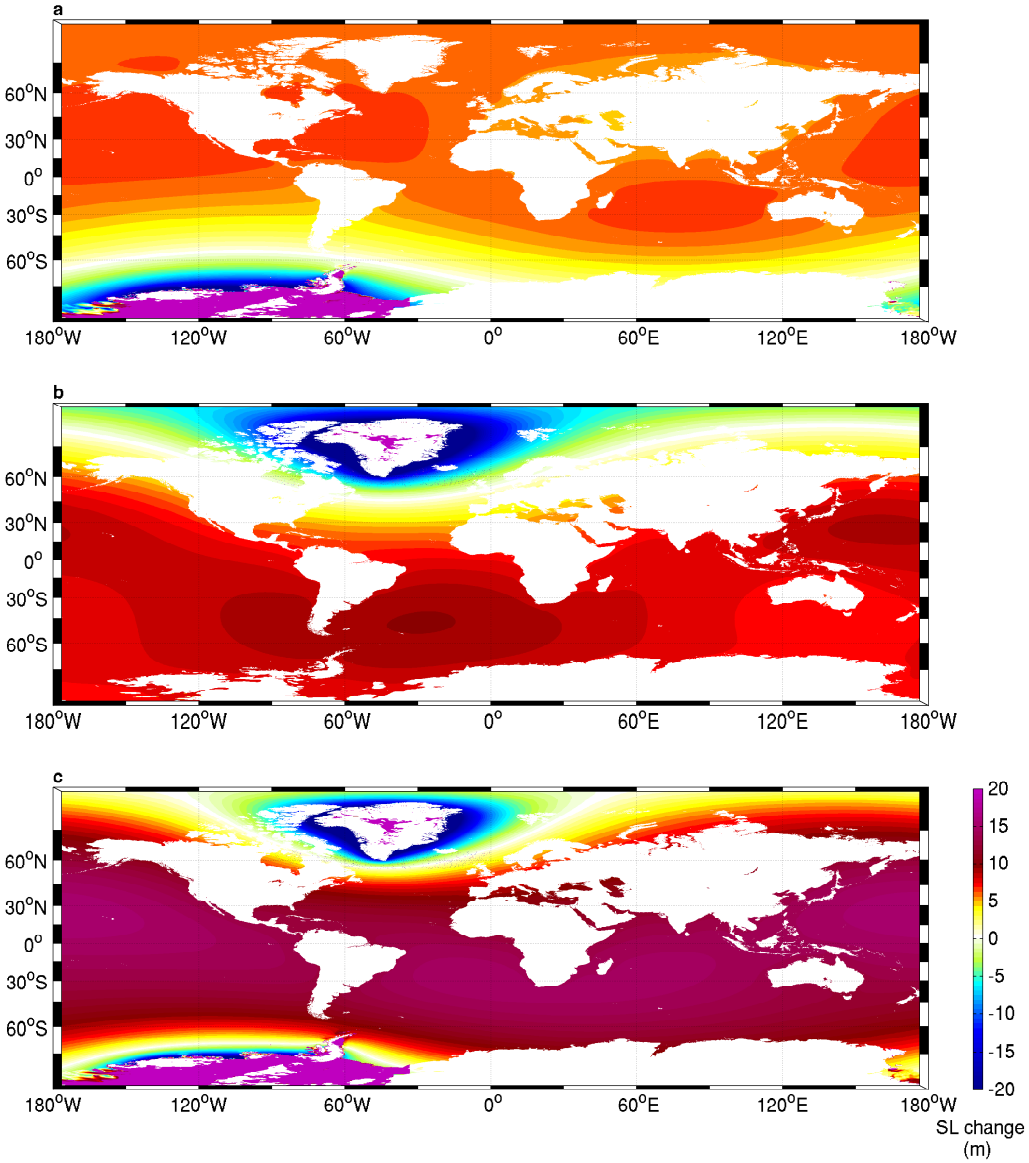

Figure 2. Sea-level change (in meters) in response to (a) a WAIS collapse (No WAIS), (b) a collapse of the GIS (No GIS), and (c) a collapse of both the WAIS and the GIS (No WAIS and No GIS). Areas where new ocean is formed due to the loss of ice from the WAIS or GIS saturate at the positive end of the color scale (purple), however, water depths for these locations are shown in Fig. 1.

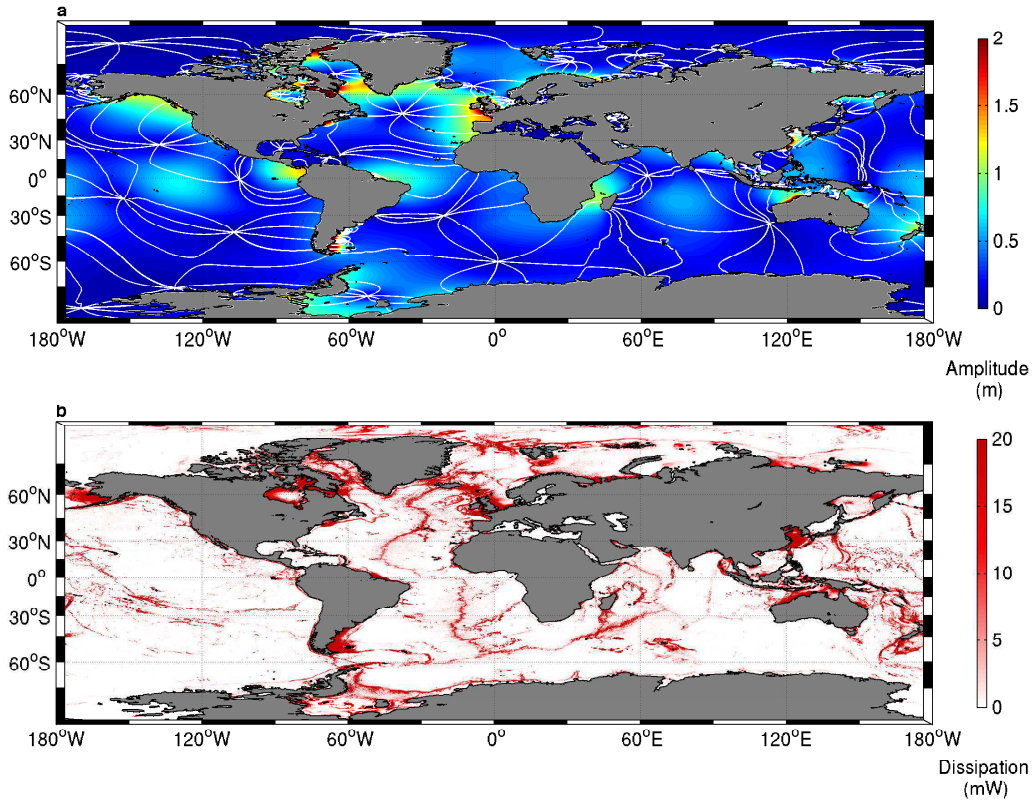

Figure 3. (a) M_2 control amplitudes (shaded) and phases (contoured in white at 1/8th M_2 period) and (b) dissipation rates.

Table 1. The control column shows M_2 tidal dissipation in shallow waters ($h < 500$ m) for selected shelf regions (the unit is GW). The other columns show the change in percent between the perturbation simulations and the control.

	control	5m SLR	No WAIS	7m SLR	No GIS	12m SLR	No WAIS & No GIS
Global	1257	7	7	15	19	16	35
Bering Sea	71	77	88	120	120	122	203
Patagonian Shelf	111	26	20	45	91	58	174
European Shelf	135	-20	-19	-23	-13	-19	-29
China Seas	180	17	17	27	34	24	25
Amazon Shelf	78	-24	-24	-27	-33	-26	-25
Coral Sea	34	53	57	86	69	75	122
East Coast of America	60	-20	-32	-23	-34	-34	-53

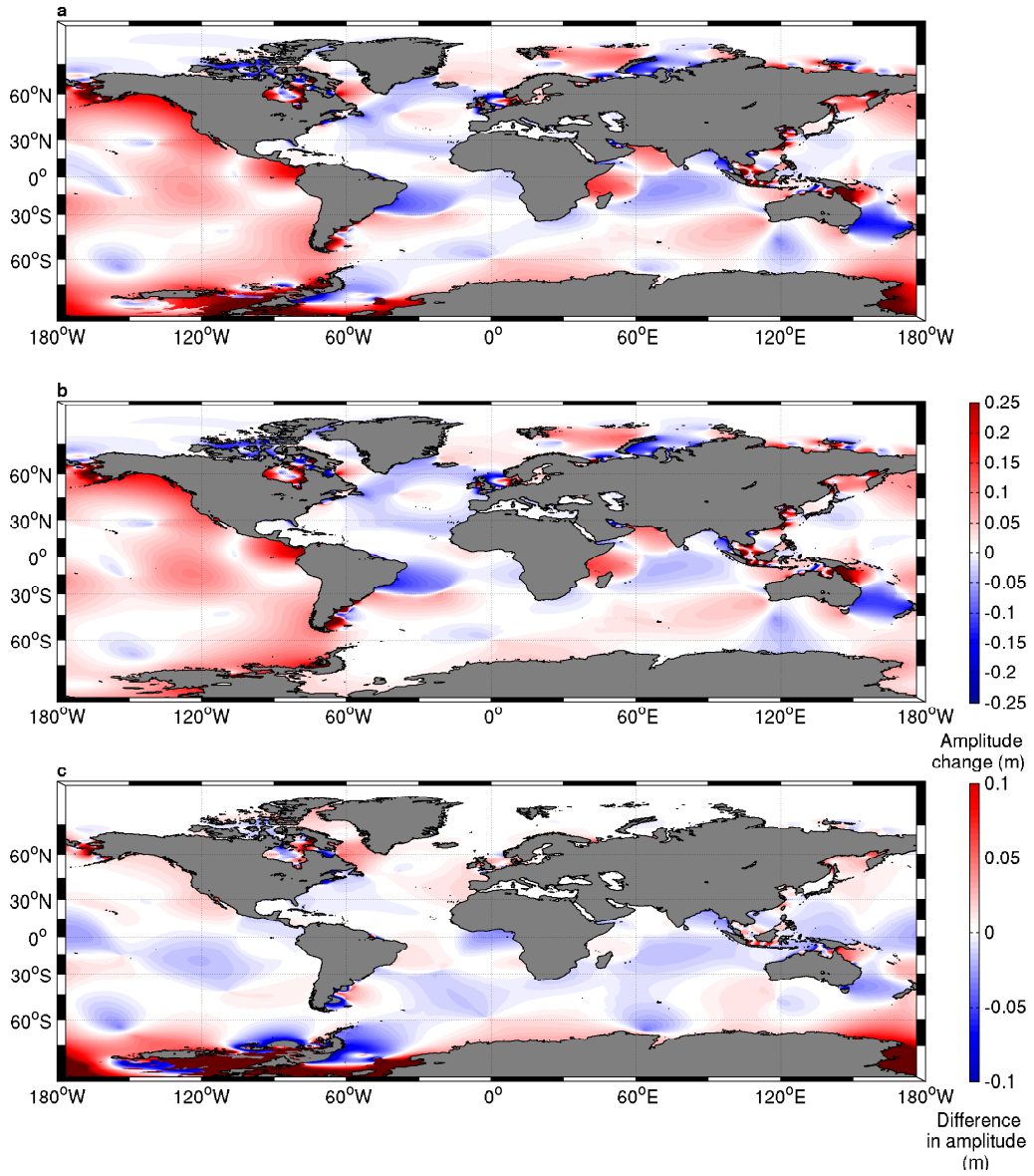

Figure 4. M_2 amplitude difference for a collapsing WAIS (in meters) compared to the control. Panel (a) shows the response to the FP SL change in Fig. 2, panel (b) shows the response of the tide to a uniform 5 m SLR, and panel (c) shows the difference in amplitude response between the FP SLR and the uniform SLR case.

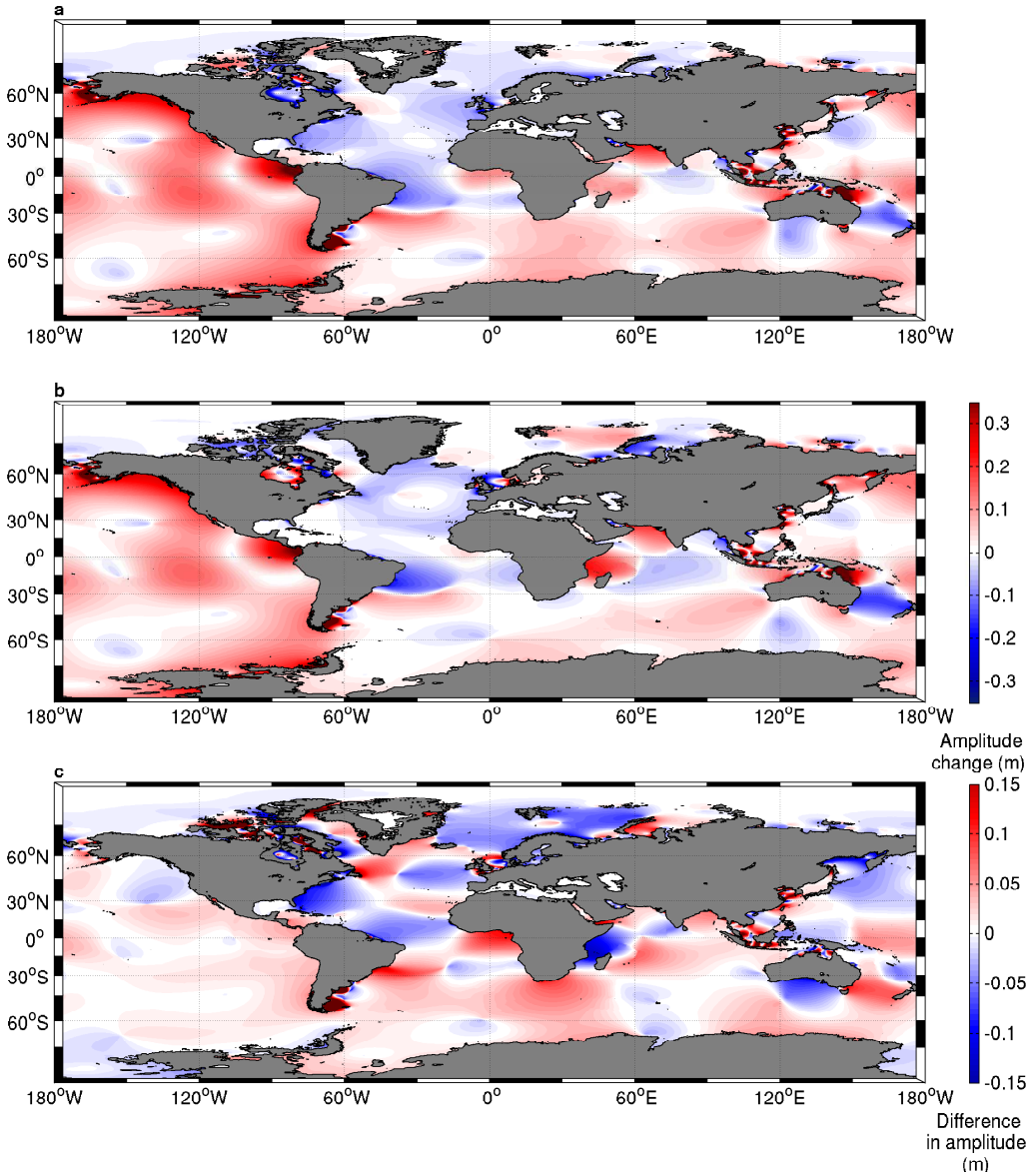

Figure 5. As in Fig. 4 but for a GIS collapse and a 7 m uniform SLR.

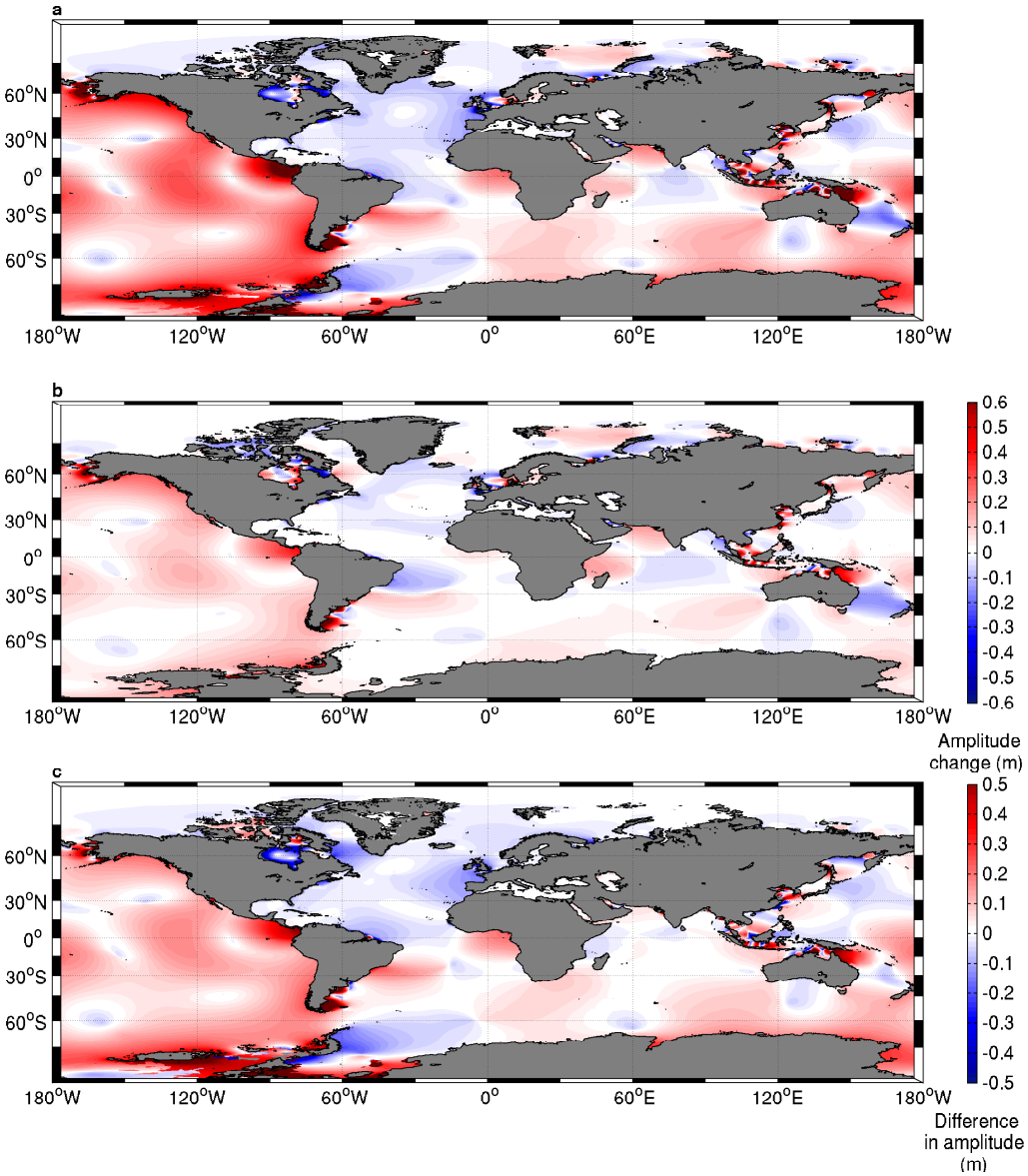

Figure 6. As in Fig. 4 but for a combined WAIS and GIS collapse and a 12 m uniform SLR.

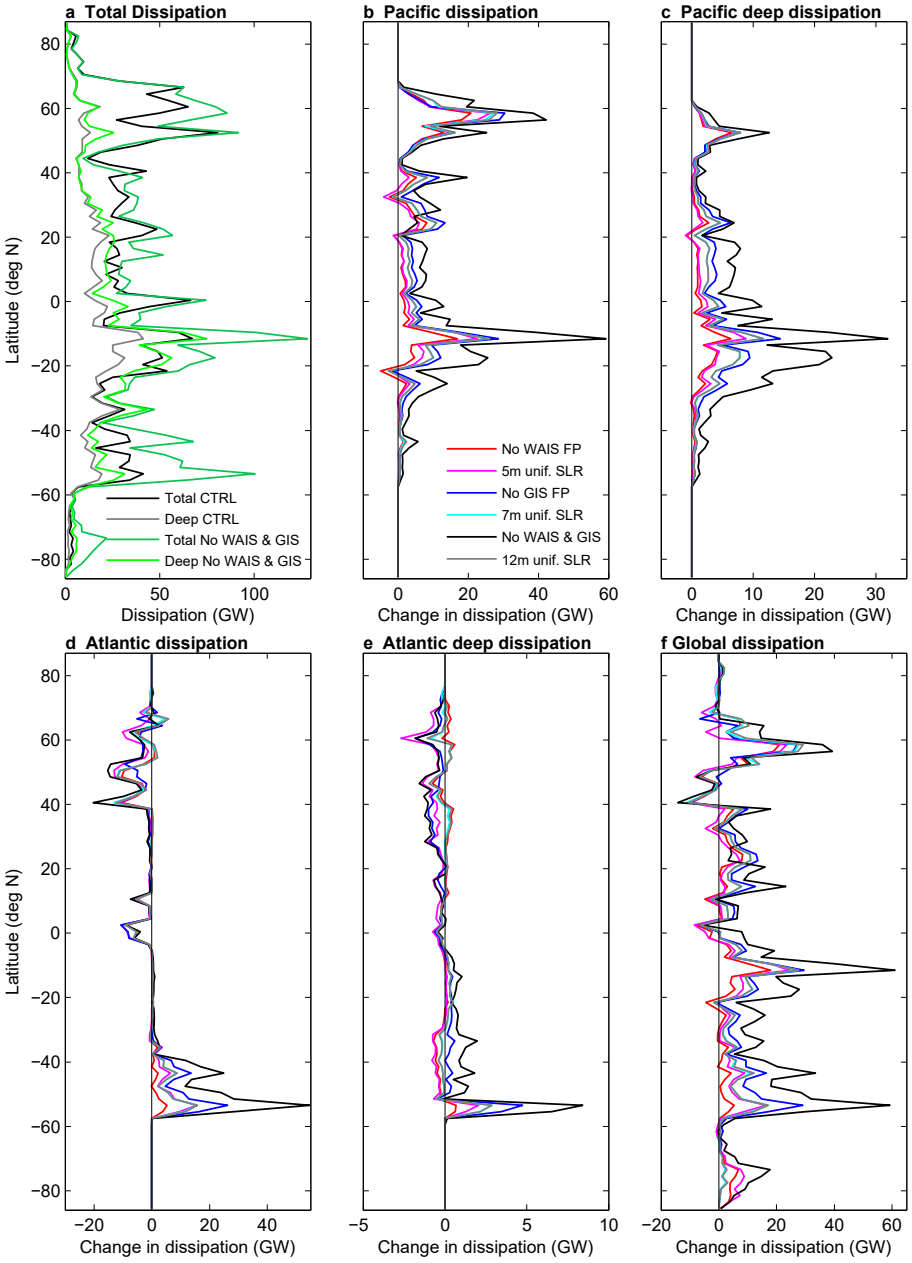

Figure 7. (a) Longitudinally integrated M_2 tidal dissipation summed over 2° of latitude for smoothing purposes for total dissipation (black) and deep dissipation (grey, $h > 500$ m). Additionally shown is the total (dark green) and deep (light green) dissipation in No WAIS & No GIS. (b-f) Change in longitudinally integrated M_2 tidal dissipation due to the ice-sheet removal for (b) total dissipation in the Pacific sector, (c) deep dissipation in the Pacific sector; (d) and (e) are the same as (b) and (c) but for the Atlantic; (f) is the same as (b) but for the global ocean.

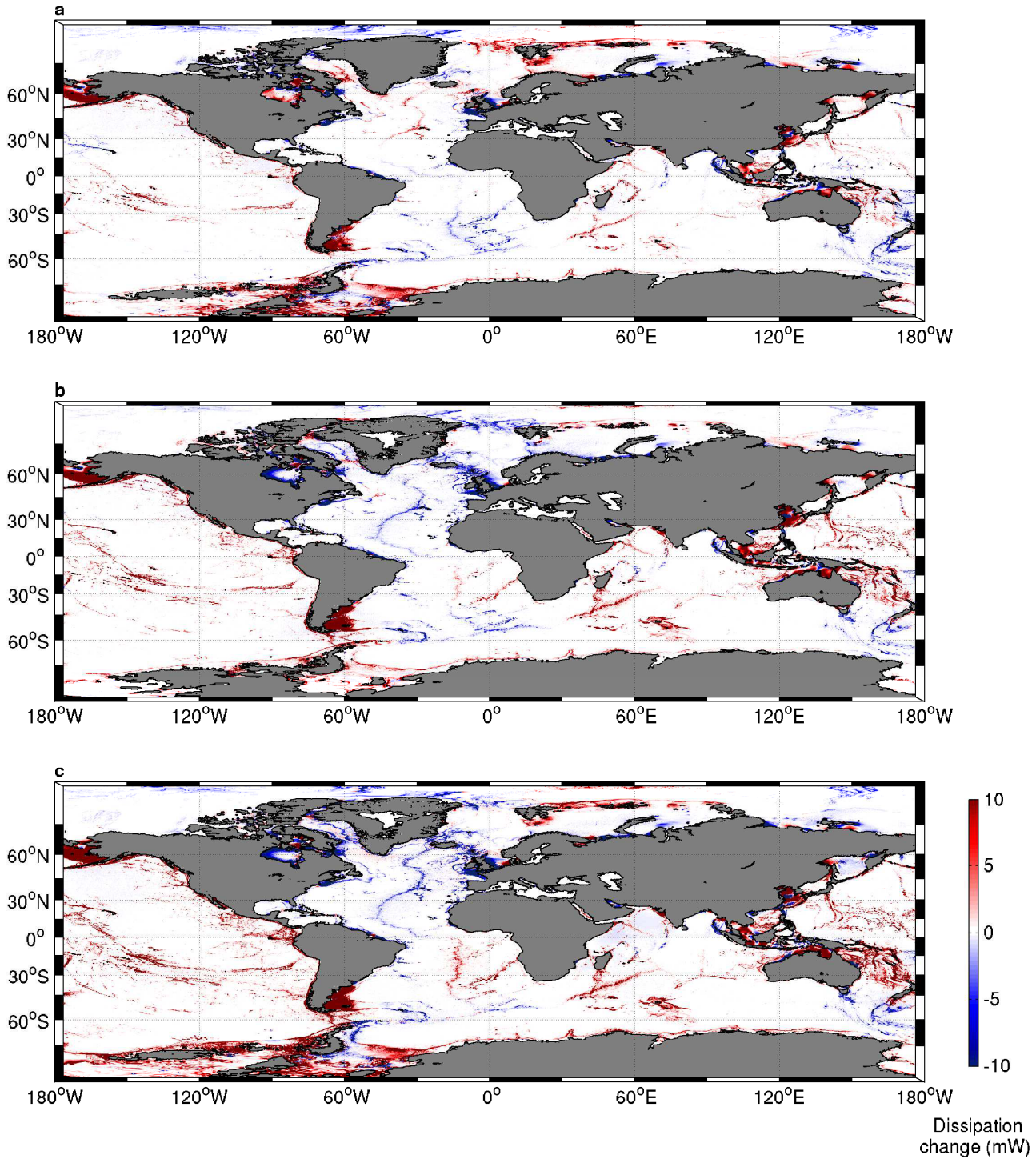

Figure 8. Change in M_2 tidal dissipation from the CTRL for (a) No WAIS, (b) No GIS and (c) No WAIS & No GIS.

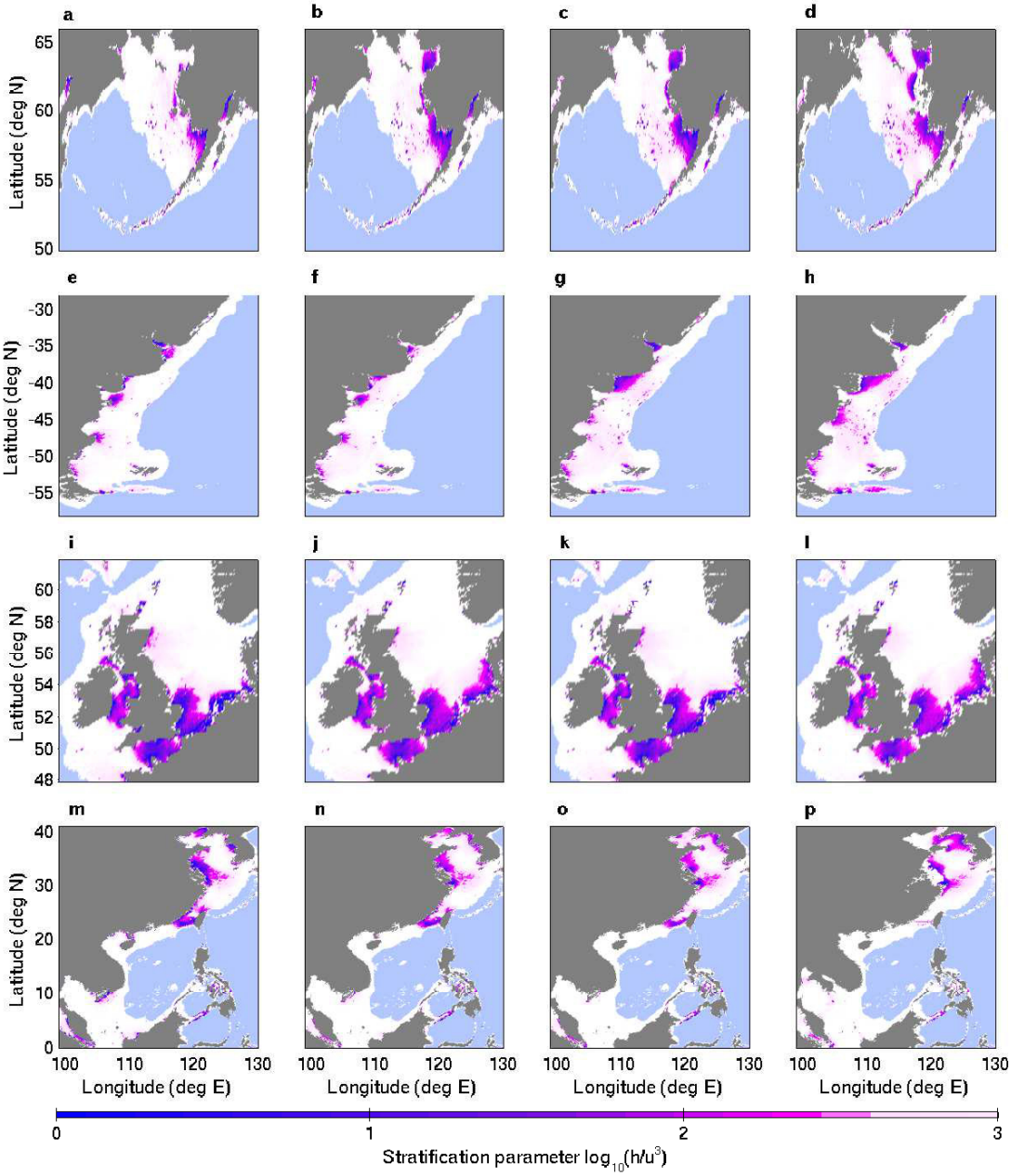

Figure 9. Shown is the stratification parameter, $\log_{10}(k)$, for the FP simulations. k was calculated using the M_2 data, and is shown for the control (first column), No WAIS (second column), No GIS (third column), and No WAIS & No GIS combined (right hand column). The light blue shading marks areas deeper than 500 m. Values below 2.5 indicate fully mixed water, values above (i.e., in white) seasonally stratified waters. Areas displayed are (first row) the Bering Sea, (second row) the Patagonian Shelf, (third row) the European Shelf and (fourth row) the China Seas.

Table 2. The control column shows the extent, in million km^2, of tidally well mixed waters in the selected shelf seas. The other columns show the change in % between the perturbation simulations and the control. Note that there are no values given for the Amazon Shelf as its oceanographic regime is dominated by freshwater fluxes and not thermal stratification.

	control	5m SLR	No WAIS	7m SLR	No GIS	12m SLR	No WAIS & No GIS
Global	2.11	-18	-20	-25	-23	-19	-18
Bering Sea	0.11	47	52	51	62	31	63
Patagonian Shelf	0.08	24	-11	24	33	25	73
European Shelf	0.19	0	3	-8	-4	-14	0
China Seas	0.39	-19	-24	-26	-30	-58	-34